

# Anisotropic Adaptation for Transonic Flows with Turbulent Boundary Layers

Kedar C. Chitale<sup>1</sup>

*University of Colorado Boulder, Boulder CO, 80309*

Onkar Sahni<sup>2</sup> and Mark S. Shephard<sup>3</sup>

*Rensselaer Polytechnic Institute, Troy, NY, 12180*

Saurabh Tendulkar

*Simmetrix Inc., Clifton Park, NY, 12065*

Kenneth E. Jansen<sup>4</sup>

*University of Colorado Boulder, Boulder, BO, 80309*

Simulation of wall-bounded turbulent flows poses significant challenges and requires tightly controlled mesh spacing and structure near the walls. Semi-structured or hybrid meshes are often used for turbulent boundary layer flows. These meshes not only account for complex geometry but also maintain highly anisotropic, graded and layered elements near the walls. However, for engineering flow problems the mesh spacing required to achieve a given level of accuracy cannot be determined *a priori* and therefore, an adaptive approach becomes essential. For wall-bounded turbulent flows, such an approach must incorporate the structure of the turbulent boundary layer and associated flow physics in order to guide the adaptive process. This paper introduces a new approach for boundary layer adaptivity, wherein flow physics indicators are used in combination with interpolation-based or numerical error indicators. The effectiveness of the current technique is demonstrated by applying them to two aerodynamic

---

<sup>1</sup> Postdoctoral Research Associate, Rensselaer Polytechnic Institute, Troy, NY, AIAA Member

<sup>2</sup> Assistant Professor, Department of Mechanical, Aerospace, and Nuclear Engineering, Troy, NY, AIAA Senior Member

<sup>3</sup> Professor, Department of Mechanical, Aerospace, and Nuclear Engineering, Troy, NY

<sup>4</sup> Professor, Department of Aerospace Engineering Sciences, University of Colorado, AIAA Associate Fellow

problems involving transonic turbulent flows.

### Nomenclature

|                |   |
|----------------|---|
| $\mu$          | Absolute or dynamic viscosity, $kg/(m.s)$   |
| $\rho$         | Density, $kg/m^3$   |
| $\nu$          | Kinematic viscosity ( $\mu/\rho$ ), $m^2/s$   |
| $(\cdot)_w$    | wall quantity (e.g., $\mu_w$ , $\rho_w$ )   |
| $P_0, T_0$     | Stagnation pressure, $Pa$ and stagnation temperature, $K$                                   |
| $\tau_w$       | Wall shear stress, $Pa$   |
| $u_\tau$       | Friction velocity ( $\sqrt{\tau_w/\rho_w}$ ), $m/s$   |
| $u^+$          | Dimensionless velocity ( $u/u_\tau$ )   |
| $y^+$          | Dimensionless length scale (wall units) ( $\rho_w u_\tau y/\mu_w$ )                         |
| $\Delta y_0^+$ | Dimensionless distance of the first point off the wall ( $\rho_w u_\tau \Delta y_0/\mu_w$ ) |
| $\delta_{99}$  | Velocity boundary layer thickness, $m$  |
| $C_p$          | Coefficient of pressure   |
| $a$            | Local speed of sound, $m/s$   |
| $b$            | Span of the wing, $m$   |
| $c_{local}$    | local chord of the section, $m$   |
| $t_0$          | Height or thickness of the first layer, $m$   |
| $r$            | Growth factor for height of two adjacent layers   |
| $n_{layers}$   | Number of layers  |
| $T$            | Total height or thickness of the layers, $m$  |

## I. Introduction

The accuracy of numerical simulations strongly depends on the mesh resolution and quality. In complex flow problems, it is difficult to determine the adequate mesh resolution *a priori*. In such

cases, an initial mesh is used to get an approximate flow solution; this mesh is then adapted using *a posteriori* error or correction indicators, i.e., based on the approximate numerical solution. This process is carried out iteratively to attain a given level of accuracy. In order for the overall adaptive process to be efficient, the resolution needs to be changed or adapted in a local fashion. This can be done by locally modifying the mesh elements based on a size field. One option is to use scalar error indicators to determine the desired mesh size field, leading to isotropic elements. However, most flow problems of interest exhibit highly anisotropic solution features such as boundary layers, shear layers, shock waves etc. These features are most efficiently resolved with anisotropic elements, i.e., where elements are oriented and stretched in a certain manner.

For viscous flows, boundary layers need to be resolved efficiently and accurately as they are a prominent flow feature. Additionally when the boundary layers are turbulent, which is often the case for high Reynolds number flows, mesh spacing needs to be properly controlled. Meshing boundary layer regions with isotropic elements will put an excessive demand on the computational resources due to an extremely large mesh. Furthermore, a fully unstructured anisotropic mesh results in poorly shaped elements (e.g., elements with aspect ratio above 1000) and in-turn leads to a numerical solution of poor quality [1]. To remedy these problems, layered, orthogonal and graded elements are used near the walls whereas the rest of the domain is filled with unstructured elements; this is referred to as a *boundary layer mesh*. Such hybrid meshes have been extensively used for flow simulations [2–7]. During adaptivity, it is desirable to maintain this layered structure of elements. Adaptation procedures based on local mesh modifications for boundary layer meshes have been presented in previous work [1]. These procedures have recently been extended to work in parallel for distributed boundary layer meshes [8].

Turbulent boundary layers have been studied extensively, both experimentally and computationally, and the mesh spacing requirements near the walls are well understood in terms of in-plane/lateral and thickness/normal resolution needs for different turbulence modeling approaches [9–11]. These near-wall resolution requirements are usually defined in a dimensionless form of wall or plus units (e.g.,  $\Delta x^+$ ,  $\Delta y^+$  and  $\Delta z^+$ ) and vary according to the modeling method (e.g., RANS, LES or DNS) and the type of wall treatment (i.e., resolved or modeled). Since the mesh spacing

requirements in the boundary layer region largely depend on the flow physics, it is advantageous to use this insight to drive the local adaptivity. Moreover, high speed flows pose additional challenges in the regions where shock waves and boundary layers interact. Mesh resolution and structure in these regions need to be carefully chosen.

This paper focuses on thickness adaptation of the boundary layer mesh. Algorithms are outlined to adaptively set or control the mesh attributes in the boundary layer regions. Strategies are included to detect and account for flow regions with separated boundary layers as well as shock wave and boundary layer interaction. The thickness control of boundary layers, wherein flow physics indicators are used, is combined with interpolation-based or numerical error indicators. The latter is also used for the interior part of the mesh, i.e., in the rest of the domain.

The article is organized as follows. Section II describes anisotropic adaptive control for boundary layer meshes. Section III outlines the new strategy for adaptive control or specification of thickness in layered portion of the mesh. Section IV illustrates the effectiveness of our approach by showcasing results for two aerodynamic problems involving transonic and turbulent flows.

## **II. Anisotropic adaptive control for boundary layer meshes**

### **A. Boundary layer mesh attributes**

Semi-structured boundary layer meshes are widely used in numerical simulation of wall-bounded turbulent flows. Such meshes provide an easy way to achieve anisotropic elements with aspect ratio of 10,000 or more, without creating poorly shaped elements which would severely influence and degrade the flow resolution. Figure 1 shows an example of a boundary layer mesh for a simple pipe geometry [8]. For 3-D meshes, the layered portion of the mesh is comprised of prisms whereas pyramids and tetrahedra are used in the unstructured or interior portion.

The boundary layer mesh contains a structure that can be decomposed into a product of a layer surface (2D) and a thickness (1D) [1]. Similarly, mesh attributes for mesh resolution needs include in-plane/lateral and thickness/normal components. The in-plane resolution is prescribed in a similar fashion as the unstructured portion of the mesh. This controls the mesh composed of triangles located on the wall (and in each layer). On the other hand, the important parameters

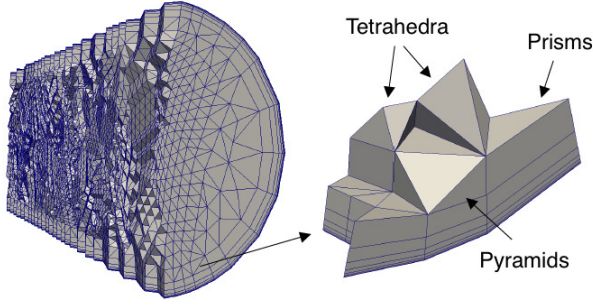


Fig. 1 Boundary layer mesh for a pipe geometry

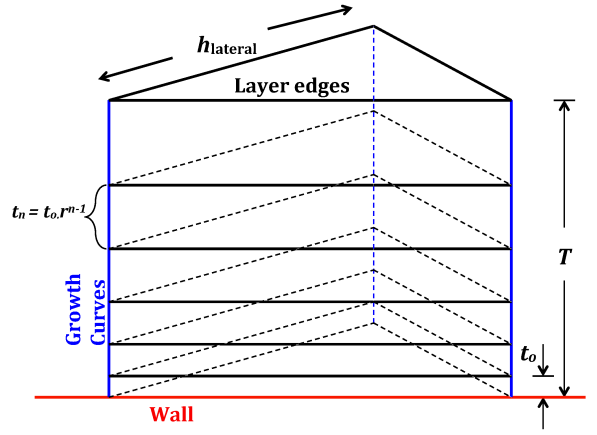


Fig. 2 Sketch of a boundary layer mesh

related to the thickness of layered portion of the mesh are:

1. First cell height or thickness (normal distance of the first mesh point off the wall surface) :  $t_0$
2. Total height or thickness of the layers:  $T$
3. Total number of layers :  $n_{layers}$
4. Growth factor in height of two layers :  $r$

Typically layers are created with a geometric progression leading to interdependence of these parameters that is given by the following equation:

$$T = t_0 \sum_{i=1}^{i=n_{layers}} r^{(i-1)} \quad (1)$$

The growth factor is the multiplication factor by which the height of a layered element increases with respect to that of the previous layer. Three of the above parameters can be chosen independently, and the fourth one is determined through Eq. 1. Figure 2 shows the general structure of a boundary layer mesh and shows some of the key mesh attributes. Out of these,  $t_0$  and  $T$  are physically the most important ones. As described in Section III, we use flow physics information from the boundary layer to set these parameters.

## B. Hessian driven anisotropic adaptivity

Outside the boundary layer, the mesh can also be anisotropic. Since the level of anisotropy required outside the boundary layer is much less, general unstructured anisotropic meshes are used and the mesh anisotropy is defined using the well-known Hessian (or interpolation error) based methods [12–15]. The anisotropic adaptivity used in this work, is based on local modifications of the mesh elements following a *mesh metric field* [16]. The mesh metric is derived from a Hessian matrix, which is a symmetric matrix constructed from the second derivatives of a particular flow solution variables. Traditionally, speed and density are chosen as the solution variables, but a combination of different variables can also be used.

The Hessian matrix is decomposed as  $H = R\Lambda R^T$ , where  $R$  is the matrix of eigenvectors and  $\Lambda$  is the diagonal matrix of eigenvalues ( $\lambda$ ). The directions associated with the eigenvectors are referred to as the principal directions and the eigenvalues are equivalent to the second derivatives along these directions. High eigenvalues are associated with higher error in the corresponding direction. Similarly, a low eigenvalue means lower error in the corresponding direction [1]. To achieve a suitable mesh resolution in different directions, a uniform distribution of local errors is applied in the principal directions which leads to  $h_k^2 |\lambda_k| = \epsilon$ , where  $\epsilon$  is a user specified tolerance for the error and  $h_k$  is the desired size in the  $k^{\text{th}}$  principal direction. More details of the size field computations can be found in Sahni et al. [17].

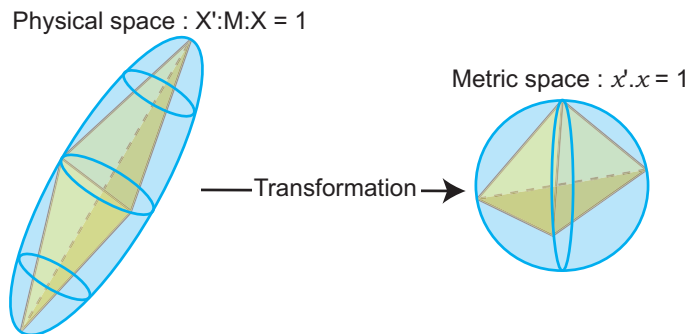


**Fig. 3 Transformation associated with the mesh metric tensor [1]**

The mesh metric field can be thought of as a transformation matrix which defines a mapping of an ellipsoid in the physical space into a unit sphere in the metric space, as shown in Figure 3. An element of any shape in the physical space is transformed to an equilateral element in the metric

space with this transformation. The goal of the mesh adaptation software is to achieve unit edge lengths in the metric space. For meshes of complex domains, this criteria is usually relaxed to constrain edge lengths in the metric space to be within an interval close to 1 [13, 16].

In this work, we use a commercial mesh generation and adaptation package provided by Simmetrix Inc. [18]. The mesh generation process employs three basic steps. In the first step the surface mesh is created on a patch by patch basis using a general purpose anisotropic triangular mesh generator. Next, an advancing front procedure is used to produce the boundary layer meshes on the selected surface patches [5]. The remainder of the domain is then filled by a general purpose anisotropic tetrahedral mesh generator. All steps in the meshing procedure interact with the original domain definition (e.g., CAD model) to ensure the correct geometric approximation of the mesh and the volume meshing steps are allowed to introduce local modifications to the surface mesh if such modifications yield a better overall mesh. The mesh adaptation procedure employs a generalized set of mesh entity splits, collapses, swaps and compound operators to convert the given mesh to one that satisfies the anisotropic mesh metric field given. The two overall steps in the mesh adaptation procedure are (i) adapting the boundary layer such that the boundary layer structure is maintained [1] and (ii) adapting the remaining interior mesh [16]. Both of these steps interact with the original domain definition to ensure the correct geometric approximation of the mesh.

### 1. *Extension to boundary layers*

The methodology outlined above works well for unstructured elements. When working with boundary layers we want to preserve their structured nature, and using this technique directly does not guarantee that. To extend anisotropic adaptivity to boundary layer meshes we instead use the approach described below.

Figure 4(a) shows a conceptual decomposition of the boundary layer mesh. The boundary layer meshes can be viewed as a product of a layer surface (2D) and a thickness (1D) mesh. The lines which are orthogonal to the wall are referred to as the *growth curves*, and the triangular surfaces parallel to the wall are referred to as the *layer surfaces*. Each layer of elements is formed with the help of the layer surfaces above and below, connected by the growth edges in between. The mesh

size on the layer surfaces is referred to as the *in-plane* or lateral size and that on the growth curves is referred to as the *normal* spacing or thickness. The ellipsoid in Figure 3 can be decomposed as an ellipse projected on the layer surface and a normal component aligned with the growth curve. This concept is shown in Figure 4(b).

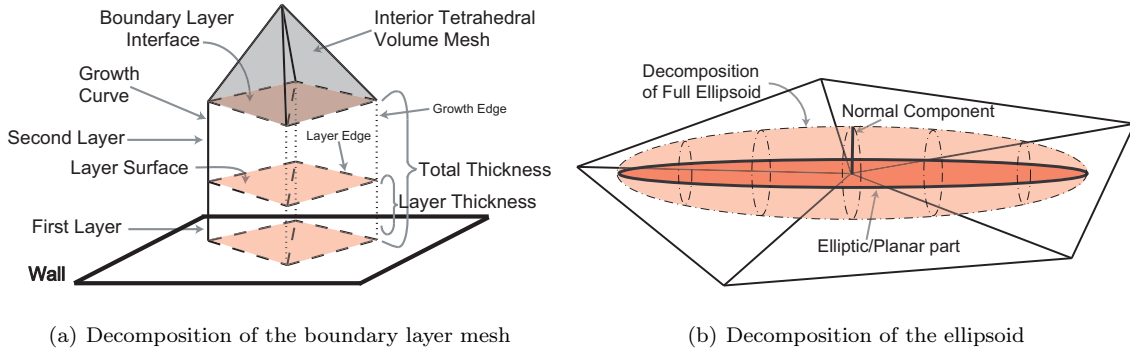


**Fig. 4 Conceptual extension of the Hessian approach to boundary layers [1]**

Adaptivity is carried out in two stages; *in-plane adaptation* that achieves the required mesh sizes on the layer surfaces and does not affect the thickness, and *thickness adaptation* which changes the normal spacing of the boundary layers. The in-plane adaptation is driven by the mesh metric field calculated from the Hessian as described in this section (see [1] for more details). The thickness adaptation is driven by the procedures outlined in the next section.

### III. Adaptive control of layer thickness

To efficiently resolve the boundary layers in turbulent flows, careful control is needed for the distribution of points in the wall-normal direction. The Hessians tend to be less accurate near the walls and therefore, they are not a good candidate to drive thickness adaptation for such a critical flow region. Since, the mesh spacings in this region are largely dictated by the boundary layer profile and the turbulence model being used, this information must be used for thickness adaptation.

To demonstrate how critical the distribution of points normal to the wall is, Figure 5 shows boundary layer profiles for a turbulent pipe flow. The first cell height is varied from  $t_0^+$  or  $\Delta y_0^+$  of 0.1 to 10. The results show inaccurate boundary layer profiles when  $\Delta y_0^+ > 5$ , with the worst profile obtained with no boundary layer mesh. These results were obtained with the Spalart-Allmaras [19]

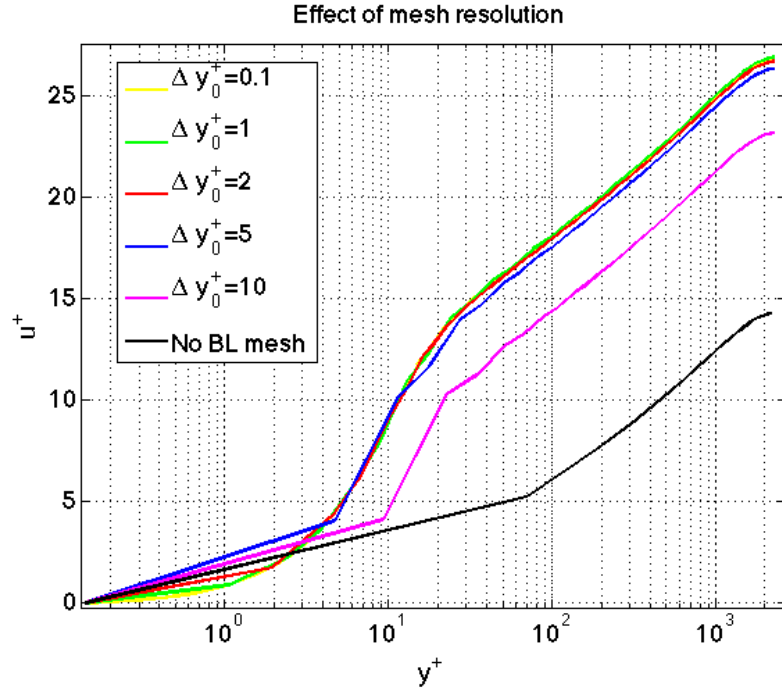


**Fig. 5** Effect of the first cell height on a turbulent boundary layer profile as predicted from the Spalart-Allmaras (RANS) turbulence model

RANS turbulence model (RANS-SA model) without any wall modeling, and with linear stabilized finite elements. This behavior would be different for other choices (e.g., turbulence model or wall modeling), however, when  $\Delta y_0^+$  is above a certain value similar trend is expected.

#### A. Types of boundary layers in flows

At this point it is important to define the different classes of boundary layers in the flow. This is because control of the mesh parameters is different for each type. The usual classification includes laminar and turbulent boundary layers. However, this paper focuses on turbulent boundary layers as they are the most prevalent type for high Reynolds number flows and are much more complex to deal with in numerical simulations. Also, the mesh spacing requirements to resolve the turbulent boundary layers are much tighter than that for the laminar boundary layers; in the former much steeper profiles or larger velocity variations are experienced near the wall (see Figure 6).

The second classification of the boundary layers relates to whether the boundary layer is attached or separated. In many flows, due to adverse pressure gradients and/or sharp turns and corners,

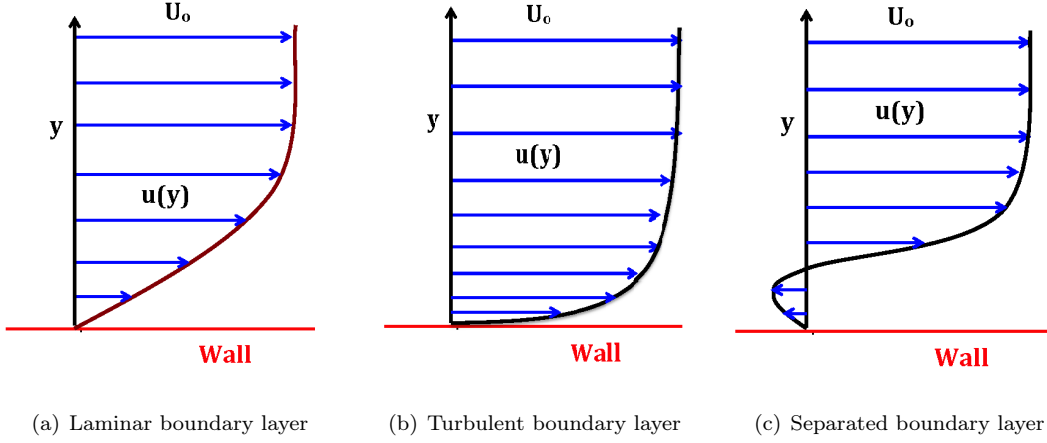


**Fig. 6 Types of boundary layer profiles**

boundary layers separate from the wall and form a separated or free shear layer. The treatment of separated boundary layers needs special care as the flow physics and mesh resolution needs in this region are different than that of the attached boundary layers. Figure 6 shows the two types of attached boundary layer profiles and a typical separated boundary layer profile. In both classifications, we use local wall shear stress to incorporate flow physics.

### B. Calculation of the wall shear stress

The near-wall mesh spacing requirements for turbulent models depend on distance from the wall in wall units ( $y^+$ ), which needs the knowledge of the wall-friction velocity  $u_\tau$ . The friction velocity can be typically calculated from the wall shear stress  $\tau_w$  as  $u_\tau = \sqrt{\frac{\tau_w}{\rho_w}}$ . Many solvers readily provide wall shear stress as a field after a post-processing step based on local gradient at the walls (e.g., finite difference or element-based gradient values). However, this typically results in numerical noise due to involvement of velocity derivative. We use an alternative method to calculate this field in a fast and an accurate manner.

Since boundary layers in high Reynolds number flows are mostly turbulent, one method to calculate  $\tau_w$  is by using the Spalding's law. It gives  $y^+$  (dimensionless wall distance) as a function of  $u^+$  (dimensionless velocity), written in an implicit form given by [20]:

$$y^+ = f(u^+) = u^+ + A[e^{(\kappa u^+)} - 1 - (\kappa u^+)^2/2 - (\kappa u^+)^3/6 - (\kappa u^+)^4/24] \quad (2)$$

where  $A = 0.1108$  and  $\kappa = 0.4$  are dimensionless constants.  $u^+$  is the dimensionless (mean)

velocity along the boundary layer and is obtained by normalizing the local velocity ( $u$ ) by the friction velocity ( $u_\tau$ ), i.e.,  $u/u_\tau$ . This law is valid through the inner layer region of an attached turbulent boundary layer on smooth surfaces and is therefore useful for wall shear stress computation since it requires information from a region very near to the wall (i.e., sublayer or buffer region of the turbulent boundary layer). Moreover, for compressible cases density changes must also be accounted inside the boundary layer (e.g., via Van Driest transformation[21]). However, for transonic cases considered in this study density changes were found to be insignificant very near to the wall, i.e., along the points taken into account for calculating the wall shear stress. For example, we observed mean density change of 0.24% and a maximum density change of 12% along the wall normal direction in the Delery bump case considered in analysis. Moreover, higher density changes very near to the wall were observed in regions where shocks and boundary layers interact; at these locations care is taken including trimming of layers as discussed later.

Using Eq. 2,  $u^+$  can be calculated at various points along the growth curve, with following iterative approach (discussed for a given point).

1. Calculate the distance of the given point on growth curve from the wall:  $\Delta y$ .
2. Retrieve the velocity at this point from the flow solution:  $u$ .
3. Guess an initial value of  $u_\tau^1$  and calculate initial  $u^+ = u/u_\tau^1$  and  $\Delta y^+ = \Delta y u_\tau^1 / \nu_w$ .
4. Use Newton's method to iteratively solve Eq. 2 until convergence is reached (to a specified tolerance) and update value of  $u_\tau$  (in each iteration).
5. Use the final value of  $u_\tau$  to calculate the final value of  $u^+$ .

This process can be repeated at any number of points on the growth curve. In the end, an average over the points gives the final friction velocity  $u_\tau$  at the wall point of the growth. We use first 3 to 5 points along the growth curves to calculate  $u_\tau$ . The wall shear stress can then be calculated as  $\tau_w = u_\tau^2 \rho_w$ . This entire process is done for each growth curve to get  $\tau_w$  at each wall vertex.

Another method to calculate a quick and an approximate estimate of the wall shear stress, is using a finite difference approach near the wall. Using the first vertex from the wall and known

$u$  and  $\Delta y_0$  values at that point,  $\tau_w$  can be calculated using  $\tau_w \simeq \mu \frac{du}{dy} \simeq \mu \frac{u}{\Delta y_0}$ . Here  $du$  equals  $u$  because the velocity is zero at the walls in the current cases. This alternative method is used for flow regions where the boundary layers are not attached and Spalding's law is not applicable.

### C. First cell or layer height ( $t_0$ )

As mentioned before, different turbulence modeling approaches have different mesh spacing requirements close to the walls. Even in the same family of turbulence models such as RANS, different approaches require varying mesh spacings depending on which specific turbulent model is used and whether the boundary layer is integrated to the wall (wall resolved approach) or if wall functions are used (wall modeling approach). The wall resolved approach makes a low Reynolds number assumption near the walls and requires that the first cell height is inside the viscous sublayer of the boundary layer ( $\Delta y_0^+ \leq 5$ ). The wall modeling approach makes suitable assumptions for near wall behavior of the boundary layer and requires that the first cell height is beyond the viscous sublayer and into the log-layer or overlap region ( $\Delta y_0^+ > 30$ ). If these requirements are not met for either of these modeling classes, then large numerical errors are incurred in turbulence calculations predicting erroneous behavior, as seen in Figure 5. However, the friction velocity, which is required to calculate  $\Delta y_0^+$ , is not known *a priori*. This makes adaptive control of the first cell height very important.

Let us assume that the turbulence model requires first cell height to be equal to  $(\Delta y_0^+)_{req}$ . If we have an initial coarse mesh with a computed solution, using the wall shear stress ( $\tau_w$ ), desired value of  $t_0$  (in a local fashion) can be calculated, by the following algorithm:

1. Get the local kinematic viscosity ( $\nu_w$ ) and desired  $(\Delta y_0^+)_{req}$  according to the turbulence model from the user (suggested values are  $(\Delta y_0^+)_{req} = 1 - 5$  for wall resolved RANS-SA,  $(\Delta y_0^+)_{req} = 30 - 50$  for wall modeled  $k - \epsilon$ ,  $0.5$  for wall resolved  $k - \epsilon$  etc.)
2. Calculate the friction velocity  $u_\tau$  as discussed in Section III B
3. Calculate the first layer height of the boundary layer by  $t_0 = \nu_w (\Delta y_0^+)_{req} / u_\tau$ .

#### D. Total height of the layered mesh ( $T$ )

It is desirable to have the total height of the layered portion of the mesh to be equal to or greater than the height of velocity boundary layer given by  $\delta_{99}$ .  $\delta_{99}$  is the distance from the wall at which the velocity becomes 99% of the local free stream velocity (i.e., at the edge of the boundary layer), and is an accepted measure of the boundary layer thickness. It is usually difficult to calculate  $\delta_{99}$  directly as it requires knowledge of a reference velocity. For simple problems (e.g., a flat plate), the reference velocity is usually the constant free stream velocity, but it can have significant local variations for problems of interest, where the flow as a whole undergoes local acceleration or deceleration. This presents a difficulty in directly calculating the boundary layer height.

To calculate  $T$ , we base our approach on the observation that vorticity outside of an attached boundary layer is negligible. Since the boundary layers have the largest velocity gradients very close to the wall, vorticity in this region is the highest and decreases as one moves farther away from the wall. As boundary layer growth curves are perpendicular to the wall (or close to perpendicular), one can walk along these edges starting from the wall, and determine the point at which the vorticity drops below a threshold value. This threshold value depends on the local maximum value of vorticity for attached boundary layers, which is most often encountered at the wall. In our analysis, we have found that a good value for the threshold is 0.02% of the wall vorticity magnitude.

#### E. Growth factor ( $r$ ) and number of layers ( $n_{layers}$ )

To increase the boundary layer elements' height away from the wall, a growth factor (also known as the stretching factor) greater than 1 is used. This is because the tightest mesh spacing is required very close to the wall, but this requirement is not as strict further away from the wall. An ideal scenario would be to achieve the height of the last layer equal to the mesh sizes in the unstructured region of the mesh in order to get a smooth transition. The mesh adaptation process provides the option of a boundary layer gradation factor, which controls the smoothness of transition of boundary layer into the unstructured part of the mesh.

There are general guidelines for what the desired growth factor should be, from the perspective of turbulence modeling. Spalart [22, 23] states that the growth factor should be close to 1.25 to

accurately capture the log-layer. Generally a growth factor beyond the value of 1.4 is deemed too large for accurately capturing the boundary layers. Many meshing tools are based on setting  $t_0$ ,  $T$  and  $n_{layers}$ , and the growth factor is automatically calculated, internally. The accuracy then in turn hinges on the knowledge and prior calculation to make sure that the growth factor being calculated is acceptable.

The adaptation tool gives the ability to set the growth factor at each wall vertex. We set  $r$  in the range of 1.2 – 1.25 to be within the acceptable limits. Selecting a growth factor less than 1.2 has the disadvantage of creating more elements than needed. The number of layers are then calculated using Eq.1.

## F. Developments for separated boundary layers

The techniques described above for calculating the different aspects of the boundary layer meshes work well for attached boundary layers. However, separated boundary layers need extra care and special detection strategies due to different flow physics that must be captured.

### 1. Extension to separated boundary layers

To treat separated boundary layers properly, they must first be detected. As it can be seen from Figure 6, they have a unique profile characterized due to flow reversal. We again make use of the wall normal growth curves and walk along the growth edges to detect a change in the flow direction. If a change (usually more than  $120^\circ$ ) is detected across the profile, then the vertex on the wall is marked as *separated*; otherwise the boundary layer is treated as an attached boundary layer.

This method requires that the total height of the layers in this region at least exceeds the height at which the flow direction is reversed. This means that typically initial boundary layer meshes for such regions should be tall enough and mesh very close to the wall should be fine enough to capture the flow reversal. Currently we make sure that this criteria is satisfied through initial meshing, but an iterative adaptive procedure like the one we use eventually leads to suitable meshes which are able to capture this effect.

### *2. Calculation of the wall shear stress*

The method of using Spalding's law to calculate the wall shear stress, is not appropriate for separated boundary layers, since the typical turbulent profile is absent. In such a case, where separation is detected, wall shear stress is calculated using the finite difference method explained earlier. The accuracy of such calculations is not as good as other methods, but it gives a reasonable estimate. Also, for separated boundary layers, the first cell height of the layer is not as crucial as for the attached boundary layers, hence such an approximate approach is justifiable.

### *3. Total height of the layered portion ( $T$ )*

For separated boundary layers, the free shear layer might get separated from the wall to a fair distance, in which case it might not be prudent to increase the boundary layer height. Even though it would be a good feature to separate or carry the layered mesh from the wall into the free shear layers in order to resolve them effectively, this capacity is still under development.

The techniques explained above for attached boundary layers predict that the boundary layer's height should be increased to the height of the complete shear layer. However, this is not always practical for separated boundary layers as this height might introduce excessive stretching of the elements near the interface.

In a more practical approach, the boundary layer height is increased beyond the height at which the flow reversal is detected so that the boundary layer mesh is tall enough to "sense" the change in the flow direction and the rest of the boundary layer mesh is destroyed and the free shear layer region is meshed with unstructured elements, with specific care to resolve the free shear layer. This approach is used in this work. For anisotropic adaptivity, velocity Hessians give good resolution in these layers since the anisotropy of the top of the shear layer is not very high.

## **G. Shock wave - boundary layer interactions**

In transonic and supersonic flows, one of the main regions of interest is where the shock waves and the boundary layers interact. Shock waves lead to sharp variations (along the shock-normal direction) and can cause thickening of the boundary layer and even separation. Due to their complex nature, these regions need greater attention and higher resolution. Since the in-plane mesh sizes for

the shock wave - boundary layer interactions are smaller, care needs to be taken to trim away the boundary layer elements that develop anisotropy in the wrong direction as the in-plane resolution becomes finer than the normal direction resolution. One way to control this, is by limiting the layer height.

We implemented a shock wave - boundary layer detection algorithm which detects a shock-boundary layer interaction by looking at the pressure gradients near the walls. The shock detection is based on the directional derivative algorithm described by Ma et al.[24]. At points very close to the walls, value of  $\nabla P$  is calculated in the flow direction. If this value is greater than a user specified threshold  $\epsilon$ , the vertex on the wall is marked as being in the vicinity of the shock. These wall vertices are marked to not increase the boundary layer height beyond a certain limit to avoid poorly shaped prism elements stretched in the normal direction. The boundary layer height in the shock region is limited by a factor of the upstream boundary layer height, so that it does not change suddenly with the shock. Though the method explained above is simplistic in nature and requires careful selection of a threshold value, it is useful in determining approximate location of a shock near a no-slip wall to limit the boundary layer height in the vicinity.

#### **H. Smoothness of fields**

Many times, coarse solutions develop non-smooth size field requests, especially in the boundary layer. The quantities like wall shear stress which form the basis of our physics based adaptivity strategy, can also be non-smooth. Mesh adaptation procedures can have a hard time handling quantities with sharp changes. A potentially unstable situation can occur if the mesh adaptation accurately adapts to such requests, since many high fidelity solvers produce oscillatory results in such cases. Due to these factors a smoothing strategy becomes necessary. In this work a smoothing strategy based on simple averaging of fields using neighboring elements is used. This smoothing technique is applied to the mesh sizes, as well as wall shear stress and the total height of the boundary layer, which are the main parameters being controlled through thickness adaptivity.

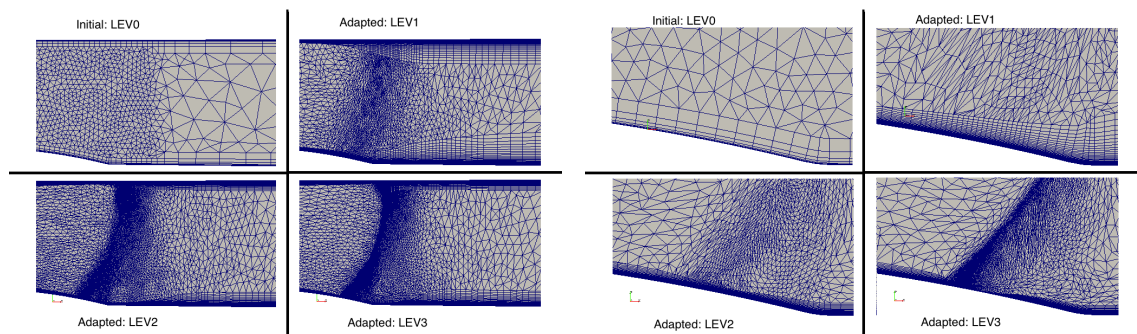
## IV. Results

In this section, we present application of our adaptive boundary layer meshing technique on two aerodynamic problems involving transonic and turbulent flows. The first case is the Delery bump [25] and the second case is the ONERA M6 wing [26]. For both of these cases, a compressible finite element formulation was used for the flow simulations [27]. The various meshes in the analysis are labeled with ‘LEV’, indicating the level of the adapted mesh, with LEV0 as the initial mesh through LEV3 which is the third adapted mesh.

### A. Delery bump

The first case we studied involves a steady transonic flow over a 2D bump which results in shock and boundary layer interaction. The experiments for this case were first carried out by Delery [25]. This case is often used to evaluate the performance of turbulence models. Air enters the nozzle from a reservoir at stagnation pressure and temperature of  $P_0 = 96000 Pa$  and  $T_0 = 300 K$ , respectively, and accelerates over the bump reaching supersonic speeds. The exit pressure is maintained at  $61500 Pa$ . For these inlet and exit conditions, a shock develops on the leeward side of the bump.

We used RANS Spalart-Allmaras [19] one-equation turbulence model for this case with wall resolved approach. The adaptivity used a combination of pressure and velocity Hessians as error indicators. The first cell height is requested to be such that  $\Delta y_0^+ = 1$ . Because the flow separates after the shock, separation detection algorithm detects this region and the boundary layer attributes are set accordingly.



(a) Initial and adapted meshes

(b) Zooms of the shock wave - boundary layer interaction zone

**Fig. 7 Initial mesh along with adapted meshes for the Delery bump case**

Figure 7(a) shows zooms of the initial mesh and the three adapted meshes towards the end of the bump. The boundary layer thickens after the shock as expected. Before the shock, boundary layer thickness remains low on both the bottom and the top walls. In the separated region, the boundary layer height is maintained until the flow reversal is detected in the boundary layer profile. The LEV1 mesh shows some overshoot in the boundary layer thickness, but latter adapted meshes show converged behavior in terms of the boundary layer height.

Furthermore, adaptive refinement follows the curved shock such that the direction normal to the shock is refined much more than that along the shock. This behavior is more evident from Figure 7(b), which displays the meshes in the shock wave - boundary layer interaction region. In adapted LEV2 and LEV3 meshes the boundary layer height is decreased in the vicinity of the shock which is in accordance to the shock detection algorithm. One thing to notice is that the initial mesh is too coarse to detect the flow reversal which occurs immediately after the shock and the boundary layer height is maintained according to the attached boundary layer algorithm. However, the adapted LEV1 mesh becomes fine enough to detect the profile change and separation is detected. Based on this the boundary layer is trimmed immediately after the shock and is maintained only until the height at which flow reversal is detected.

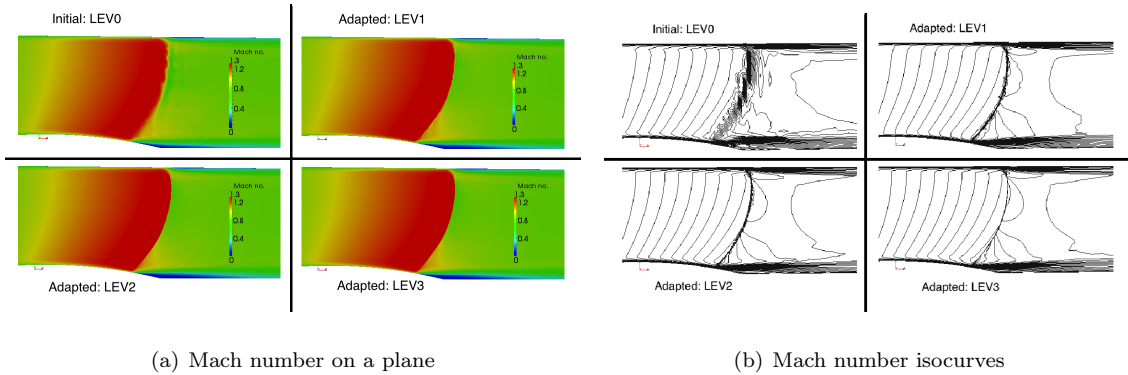
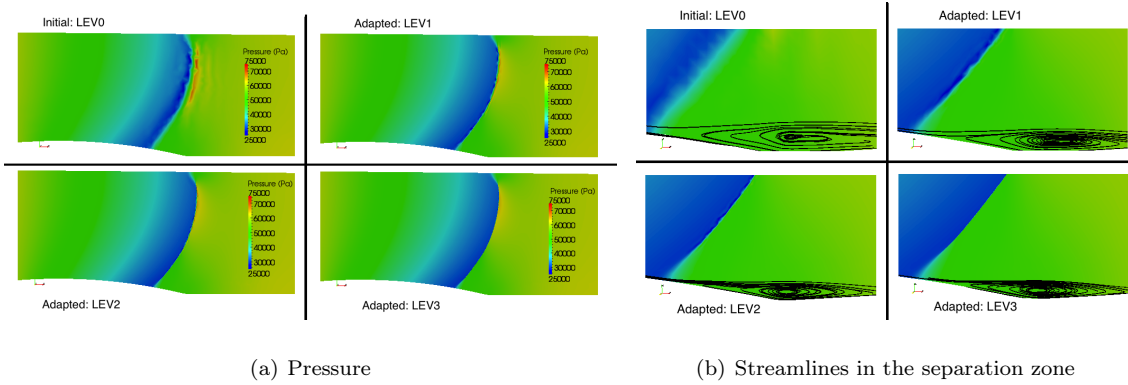


**Fig. 8 Mach number and isocurves for the Delery bump case**

Figure 8 shows Mach number on a plane as well as its isocurves. The isocurves show progressive sharpness in the shock region, with adaptivity (on LEV2 and LEV3). The LEV3 mesh gives the sharpest resolution. Figure 9(a) shows pressure around the shock region over the bump. The adapted meshes are able to resolve the shock sharply as compared to the initial mesh; the best resolution is given by the LEV3 mesh. Figure 9(b) shows a zoom of the shock wave - boundary



(a) Pressure (b) Streamlines in the separation zone  
**Fig. 9** Pressure on a plane with a zoom of the shock-boundary layer interaction zone and the separation bubble

layer interaction zone and streamlines in the local separation or recirculation bubble induced by the shock. The location of the interaction zone is better predicted in the adapted meshes. The initial mesh over predicts the size of the the separation bubble, which is improved with the adaptivity. The LEV2 and LEV3 meshes show similar behavior of the streamlines, indicating mesh convergence. This aspect is studied in more detail below.

To show effectiveness of adaptivity in adjusting the first cell height from the wall, we plot a bar graph showing distribution of  $\Delta y_0^+$  distance of all first layers against % occurrence for different meshes, see Figure 10. The initial LEV0 mesh was meshed with a uniform first cell height for all walls and it shows no specific behavior. More than 50% of the first cell heights lie beyond  $\Delta y_0^+$  of 5, which is not ideal for the turbulence model we use (with no wall model). With adaptation we see significant improvements in this behavior. For the LEV1 mesh nearly 70% of the first cells have height (in wall units) below or close to 1. This number increases to 97% for the LEV2 mesh and 99% for the LEV3 mesh, with majority of them close to 1. However, some first cells have height below 1 (in wall units) due to numerical estimation of quantities that are used in our adaptive procedures and also due to application of limiting layer height in the separation region.

The normalized bottom wall pressure is plotted in Figure 11 and indicates a good agreement between the experimental and the simulation values for initial and adapted meshes. The flow solver over predicts the wall pressure after the shock, in the separation zone. This behavior has been seen before by Emory et al. [28] and Lien et al. [29]. These differences can be attributed to the three dimensional nature of the experiment and to the turbulence model's limitations in capturing the

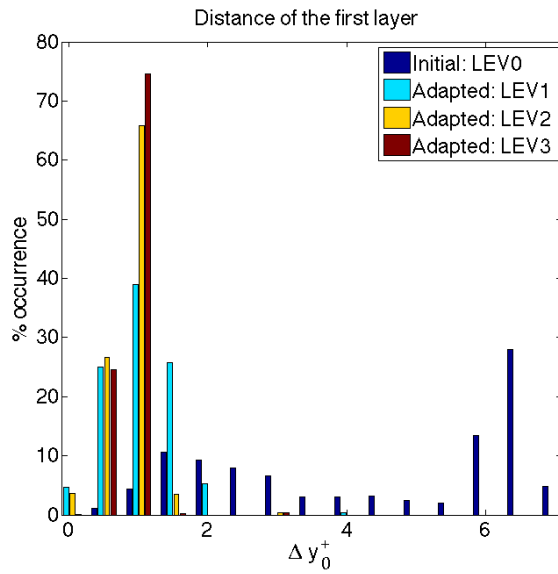


Fig. 10 First cell heights for the initial and adapted meshes

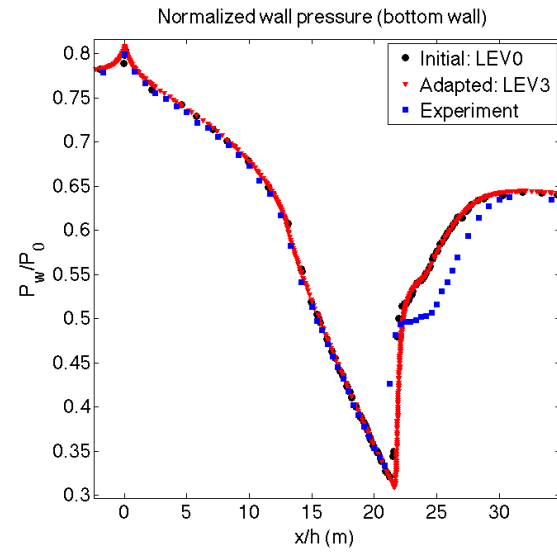


Fig. 11 Normalized wall pressure on the bottom wall

| Mesh                | Separation point<br>(x/h) | Reattachment<br>point (x/h) |
|---------------------|---------------------------|-----------------------------|
| Initial mesh (LEV0) | 22.33                     | 26.60                       |
| Adapted mesh (LEV1) | 22.08                     | 26.66                       |
| Adapted mesh (LEV2) | 22.15                     | 27.08                       |
| Adapted mesh (LEV3) | 22.14                     | 27.16                       |
| Experiments [25]    | 21.84                     | 27.04                       |

Table 1 Separation and reattachment locations (normalized by the bump height)

effect of separation, which is not a concern of this paper.

Table 1 lists the separation and reattachment points for different meshes. The distance values are normalized by the height of the bump ( $h$ ), which is  $12\text{mm}$ . The initial mesh predicts delayed separation and earlier reattachment than the experiment values. The adapted meshes, especially LEV2 and LEV3, give a better agreement with the experimental results.

Boundary layer profiles are plotted in Figure 12 along various streamwise locations. Figure 12(a) and 12(b) show boundary layer profiles in the separation zone after the shock. The initial mesh

is not able to capture the correct behavior due to its coarse resolution in this region. The adapted LEV3 mesh shows much better agreement with the experimental values in the separation zone. This is particularly important because in the separation zone, we are limiting the height of the boundary layers. For the boundary layer profiles after reattachment shown in Figure 12(c) and 12(d), adapted and initial meshes both give good approximations to the profile.

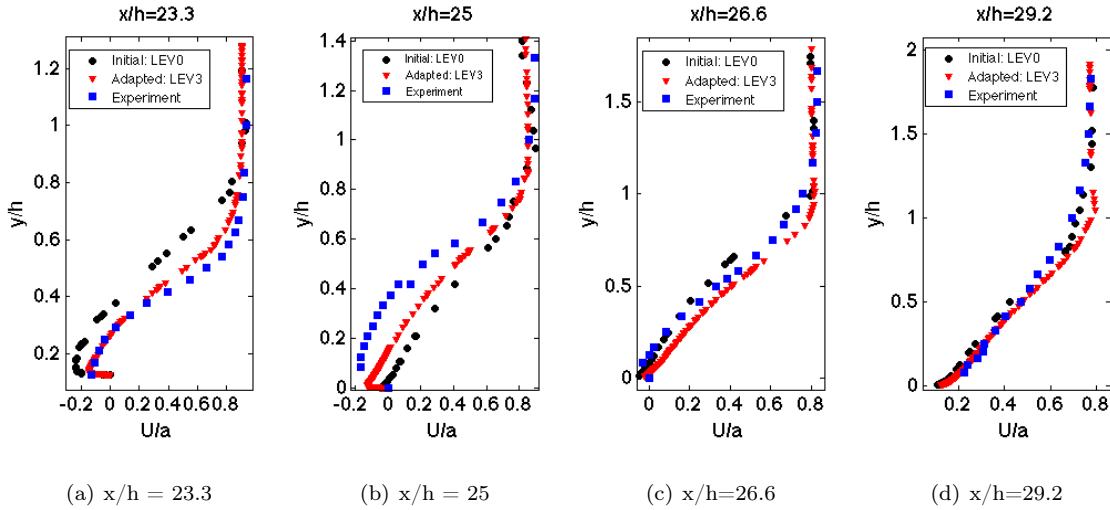


Fig. 12 Boundary layer profiles at various streamwise sections for the Delery bump case

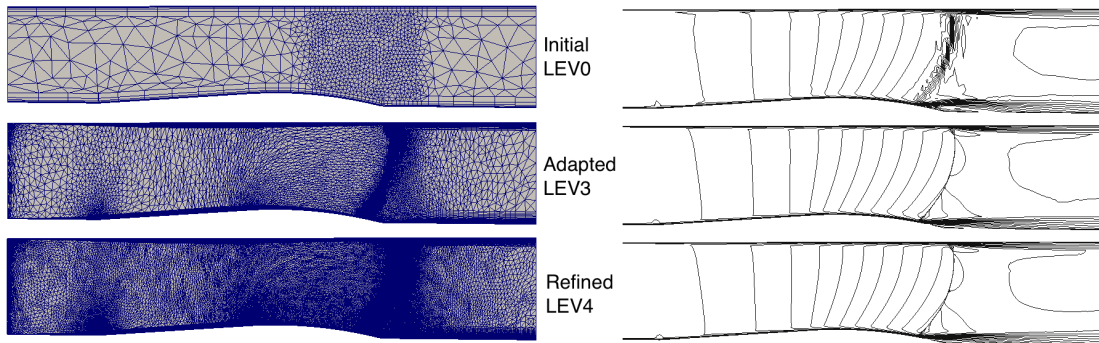


Fig. 13 Initial LEV0, adapted LEV3 and uniformly refined LEV4 meshes and corresponding Mach isocurves

To make sure mesh convergence was reached, we uniformly refined the LEV3 mesh. This means that each mesh edge was split into two to get a new LEV4 mesh. This LEV4 mesh showed no significant difference in the solution when compared to the LEV3 mesh, which makes a strong case for verification of the results. Figure 13 shows the LEV4 mesh generated with uniform refinement in comparison to the initial LEV0 and the adapted LEV3 mesh. The Mach isocurves on the right

show no significant difference in their behavior, displaying that mesh independence is reached. This indicates that any further mesh refinement beyond the LEV3 mesh would produce similar results with no significant differences.

*1. Comparison with nested refinement*

To display the effectiveness of adaptive refinement approach, we compared it with nested refinement of the Delery bump (denoted by NLEV). In nested refinement, each mesh edge is split in two. Typically, the layers are not refined in the direction of the growth curves, meaning that the normal spacing is kept constant. The first two refinement passes are done with this approach. However, sometimes there is also a need to change the normal spacing of the boundary layers to check if that has any effect on the flow solution. With the adaptive tools that we use, this can be achieved by converting the prisms and pyramids in the boundary layers to tetrahedra. In the last nested refinement pass, the normal spacing is also changed using tetrahedra elements in the boundary layers.

Clearly, the coarse initial mesh (LEV0) that we used in the adaptive approach is inadequate to capture the shock. While it was useful in showing that we could start with such a mesh and still arrive at a converged solution on the third adapted mesh, for the nested refinement approach we start with a mesh which is more refined (preemptively) in the area near the leeward side of the bump (NLEV0). Nested refinements are then carried out and solution is computed after each refinement pass and the solution is compared to the adapted LEV3 mesh. The NLEV3 and LEV3 meshes give similar flow solution when visualized.

The number of points/vertices and cells/elements of the adapted meshes and the uniformly refined meshes, and the time required to create them are given in Table 2. As uniform refinement is a fairly straight forward operation, the time required to create refined NLEV meshes is smaller compared to adapted LEV meshes, considering the number of elements added in each cycle. Even though it takes less time to create the NLEV meshes, the time taken for adaptation/refinement is usually only a small fraction of the time required for flow analysis. Since adaptation creates meshes with significantly smaller number of elements, the analysis time is reduced by a greater margin and

is therefore a preferred method to refine the meshes. For example, the refined NLEV3 mesh has 85.16 million elements compare to the adapted LEV3 mesh that has 1.78 million elements and takes nearly 682 CPU hours to compute 100 time steps, whereas the latter requires only 7.6 CPU hours for the same.

| Mesh                | # elements<br>(million) | # vertices<br>(million) | CPU time to<br>create (min) |
|---------------------|-------------------------|-------------------------|-----------------------------|
| Adapted mesh: LEV1  | 0.60                    | 0.12                    | 1.50                        |
| Adapted mesh: LEV2  | 1.05                    | 0.21                    | 25.91                       |
| Adapted mesh: LEV3  | 1.78                    | 0.33                    | 32.48                       |
| Refined mesh: NLEV1 | 1.25                    | 0.28                    | 0.40                        |
| Refined mesh: NLEV2 | 10.02                   | 1.83                    | 3.21                        |
| Refined mesh: NLEV3 | 85.16                   | 16.72                   | 13.65                       |

**Table 2 Computational comparison of meshes**

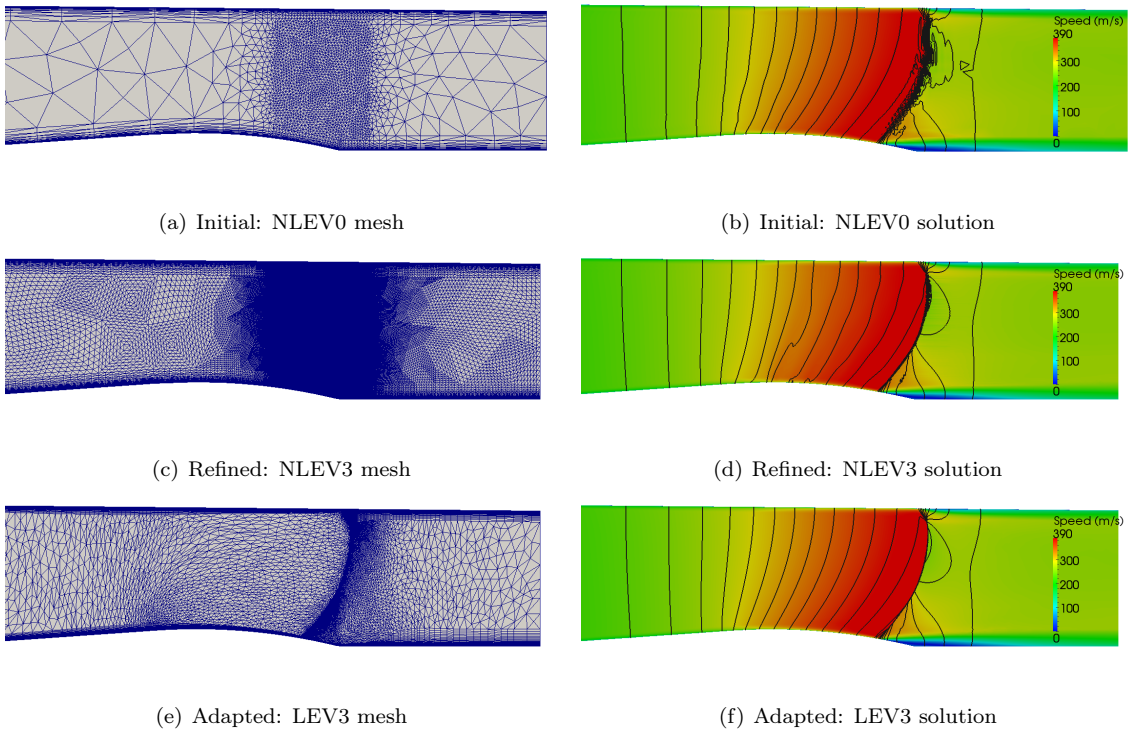


**Fig. 14 View of the meshes and corresponding speed and pressure isocurves for the refined NLEV3 and adapted LEV3 meshes**

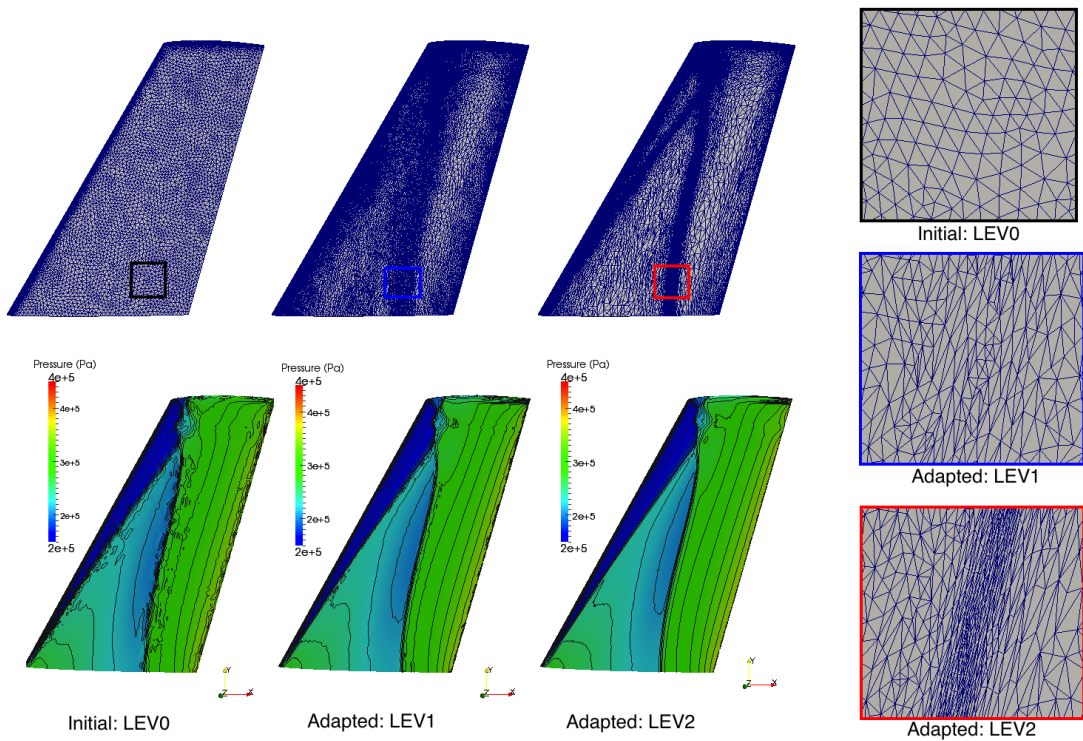
Figure 14 shows the refined NLEV3 and the adapted LEV3 meshes over the bump along with corresponding speed isocurves in color and pressure isocurves as black lines. Note that the layers in the refined NLEV3 mesh are converted to all tetrahedra elements to uniformly refine the wall normal direction. Though the adapted LEV3 mesh shows prism boundary layers, for a fair comparison in terms of computational resources, it was also converted to all tetrahedra elements and those statistics have been used in Table 2. From the mesh pictures it is clear that the reason for the efficiency given by the adapted mesh is due to the selective refinement of the shock region and the anisotropy which develops as a result. The other flow regions remain comparatively coarse for the adapted LEV3 mesh, which contribute to the computational savings, whereas for the nested refinement all regions are uniformly refined.

From the computed solution the location and the shape of the shock look fairly similar for both the meshes, at this level of visualization. The sizes of the separation bubble predicted by both meshes agree well with each other. This indicates that both the adapted LEV3 and refined NLEV3 meshes give very similar results. However, computationally these two meshes are vastly different and using the adapted mesh leads to significant savings in terms of the computational resources. This demonstrates the efficiency and the effectiveness of the present adaptive approach.

## B. ONERA M6 wing

The ONERA M6 wing is one of the classic validation cases. The reference experimental data is from Schmitt and Charpin in 1979 [26]. Air enters the wind tunnel at transonic speed and is accelerated over the wing to supersonic speeds causing a shock to appear on the upper surface of the wing. The free stream Mach number is 0.84, and the angle of attack is  $3.06^\circ$ . The free stream pressure and temperature are 42.89 *psi* and 255.5 *K*. The Reynolds number is 11.72 million based on the mean aerodynamic chord. This flow demonstrates a strong need for adaptive meshes due to its unknown shock location *a priori* to the flow solve and complex nature of the lambda shock.

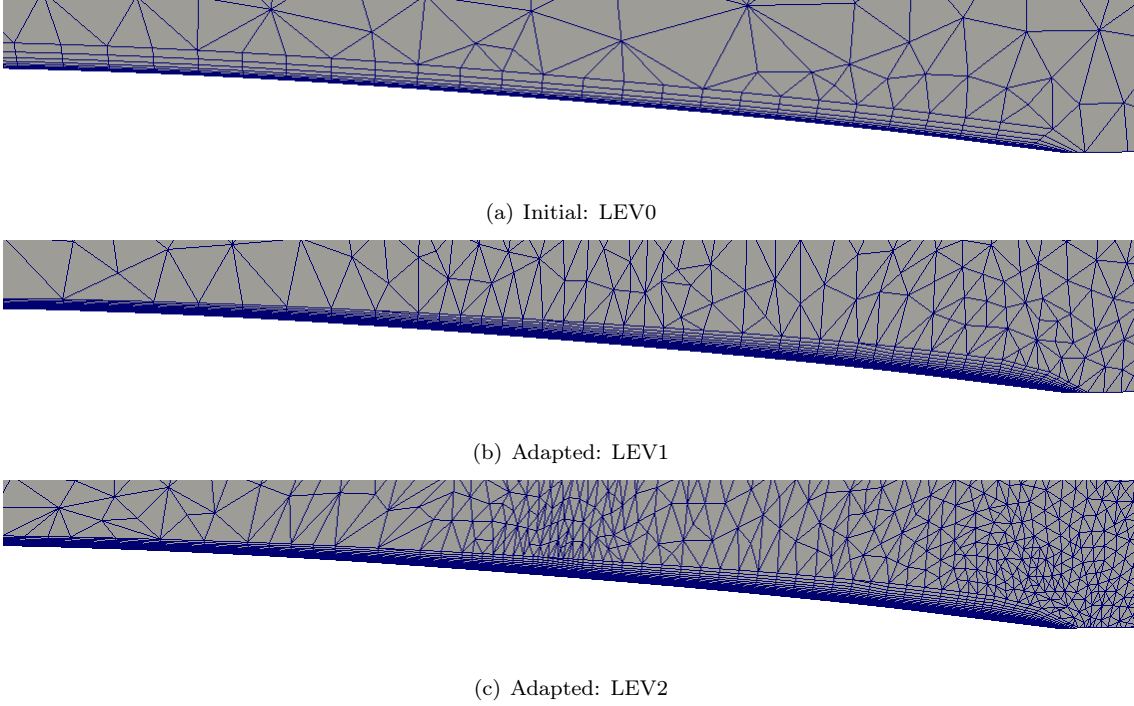
For this case too, we used the Spalart-Allmaras [19] one-equation turbulence model. Pressure Hessians were used as error indicators to resolve the shock on the wing surface. The first cell height was requested to be  $\Delta y_0^+ = 1$ .



**Fig. 15 Meshes and corresponding surface pressure plots and isocurves**

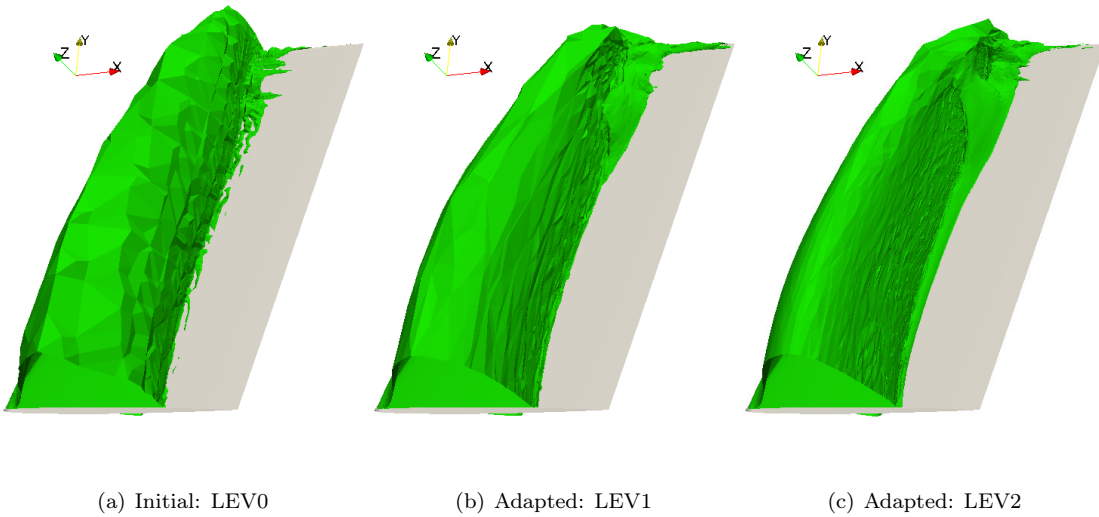
Figure 15 shows the initial and the adapted meshes of the wing surface and the corresponding surface pressure. The mesh gets refined in the shock region and the lambda shape of the shock is clearly replicated in the adapted meshes. The mesh downstream of the shock is coarsened, due to low values of pressure gradients in this region. The surface pressure isocurves become sharper and more regular in shape with adaptivity. On the right hand side of Figure 15, zoom near the shock region is shown, where anisotropy is developed in the surface elements along the shock as compared to the direction normal to the shock. One thing to notice is that the elements start aligning themselves with the shock in the adapted LEV1 mesh, but need one more adaptation loop to show this behavior more clearly.

Figure 16 shows the changes in the boundary layer height on the upper surfaces of the wing with adaptivity. Clearly, the total height of the boundary layer prior to the shock remains relatively low. After the shock the boundary layer thickens as expected. The zone where shock wave meets the boundary layer can also be seen and the elements oriented with finer resolution normal to the shock and longer edges along the shock are clearly visible. The average first cell layer height for the



**Fig. 16 Change in the boundary layer height on upper surface of the wing**

initial LEV0 mesh in terms of  $\Delta y_0^+$  is 8.2, for the adapted LEV1 mesh it is 1.3 and for the adapted LEV2 mesh it is about 1.1, which shows that thickness adaptation is able to get the first cell height close to the requested value of  $\Delta y_0^+$  of 1.



**Fig. 17 Isosurface of Mach number at unity for the initial and the adapted meshes**

Figure 17 shows isosurface of Mach number equal to unity on the upper side of the wing. The anisotropy developed in the spanwise direction is replicated in the Mach isosurface. In general, the

adapted meshes show smoother surfaces indicating higher degree of resolution as compared to the initial mesh.

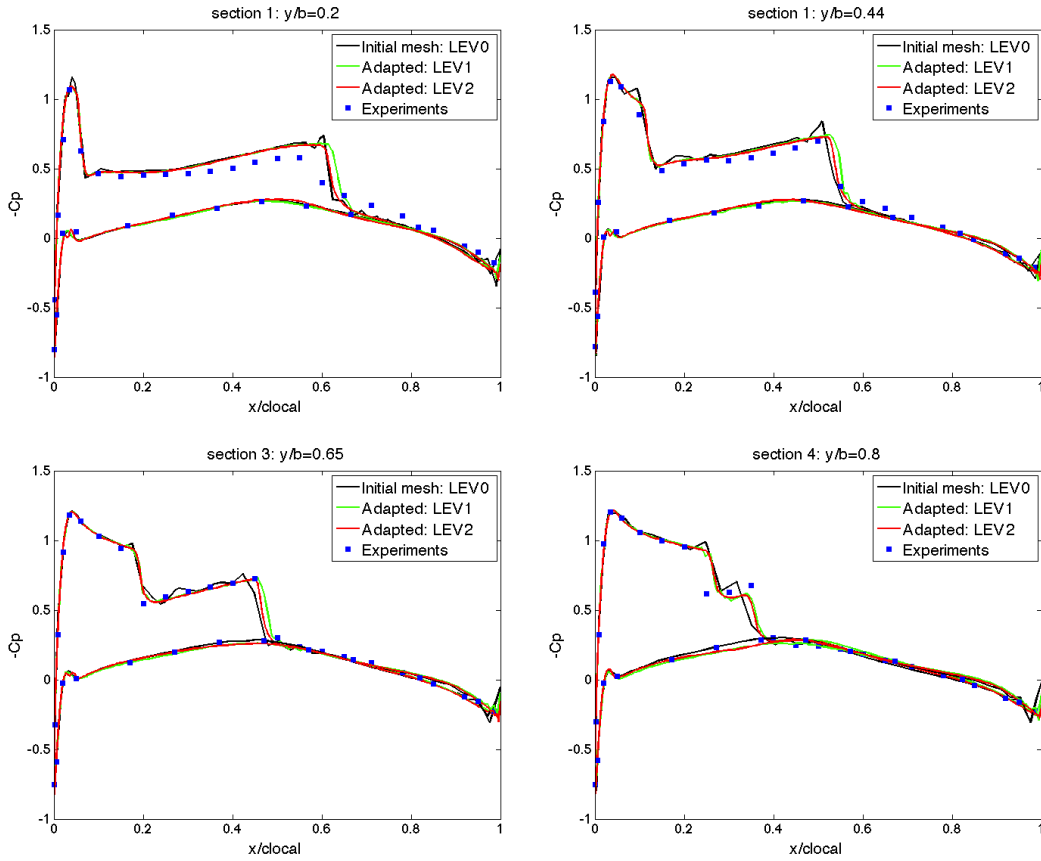


**Fig. 18** Coefficient of pressure on the wing at various spanwise sections

Figure 18 shows coefficient of pressure plots for different spanwise sections of the wing. The initial mesh shows some overshoot near the shock which is expected due to its coarse nature. Adaptivity removes this problem and gives  $C_p$  values which match the experimental data. One particular area of interest is the shock on section 4 ( $y/b = 0.8$ ), which is in fact a double shock. The adapted meshes are able to capture this double shock structure. Overall, for ONERA M6 wing case the adapted meshes give sharper shock resolution than the initial mesh. The  $C_p$  values agree well with the experiments and improve with adaptivity.

## V. Conclusion

In this paper we have presented anisotropic adaptive control of boundary layer meshes and their application to transonic turbulent flows. A new way to adaptively calculate the attributes of

boundary layer meshes is described and is combined with the traditional numerical error indicators to drive overall mesh adaptivity. A clear advantage of such an approach is the use of flow physics to set normal mesh spacings near the walls, instead of using less effective error indicators.

We demonstrated the ability of this approach to capture the boundary layer physics as well as other flow regions by applying the adaptive techniques to two transonic flow cases. The first application was the Delery bump, where adaptivity improved the shock resolution and the boundary layer profiles. The separation zone was captured with greater accuracy with adaptivity. A uniform refinement of the adapted mesh was used to verify the adaptivity approach arrived at a mesh independent solution. The second application was the ONERA M6 wing, where also adaptivity leads to better results in terms of the surface pressure isocurves and the coefficient of pressure on the wing. We also showed that the shock wave-boundary layer interactions are captured better with adapted boundary layer meshes.

#### **Acknowledgments**

The work was carried out at University of Colorado Boulder, in close collaboration with Simmetrix, Inc., NY and Rensselaer Polytechnic Institute, NY, and was supported by the NASA STTR Phase II Grant No. BEE103/NNX11CC69C.

This work utilized the Janus supercomputer, which is supported by the National Science Foundation (award number CNS-0821794) and the University of Colorado Boulder. The Janus supercomputer is a joint effort of the University of Colorado Boulder, the University of Colorado Denver and the National Center for Atmospheric Research. Resources at the Computational Center for Nanotechnology Innovation (CCNI) at Rensselaer were also used for testing and development.

#### **References**

- [1] Sahni, O., Jansen, K. E., Shephard, M. S., Taylor, C. A., and Beall, M. W., “Adaptive boundary layer meshing for viscous flow simulations,” *Engineering with Computers*, Vol. 24, No. 3, 2008, pp. 267–285.
- [2] Pirzadeh, S., “Unstructured viscous grid generation by advancing-layers method,” *AIAA Journal*, Vol. 32, 1994, pp. 1735–1737.

- [3] Connell, S. and M.E., B., “Semistructured mesh generation for three-dimensional Navier-Stokes calculations,” *AIAA Journal*, Vol. 33, No. 6, 1995, pp. 1017–1024.
- [4] Marcum, D., “Generation of unstructured grids for viscous flow applications,” *AIAA paper 1995-0212*, 1995.
- [5] Garimella, R. V. and Shephard, M. S., “Boundary layer mesh generation for viscous flow simulations,” *International Journal for Numerical Methods in Engineering*, Vol. 49, 2000, pp. 193–218.
- [6] Loseille, A. and Löhner, R., “Robust Boundary Layer Mesh Generation,” *Proceedings of the 21st International Meshing Roundtable*, 2013, pp. 493–511.
- [7] Ito, Y., Murayama, M., Yamamoto, K., Shih, A., and Soni, B., “Efficient hybrid surface/volume mesh generation using suppressed marching-direction method,” *AIAA Journal*, Vol. 51, No. 6, 2013, pp. 1450–1461.
- [8] Ovcharenko, A., Chitale, K., Sahni, O., Jansen, K. E., and Shephard, M., “Parallel Adaptive Boundary Layer Meshing for CFD Analysis,” *Proceedings of the 21st International Meshing Roundtable*, 82, IMR, 2012, pp. 437–455.
- [9] Jansen, K. E., “A stabilized finite element method for computing turbulence,” *Computer Methods in Applied Mechanics and Engineering*, Vol. 174, No. 3-4, 1999, pp. 299–317.
- [10] Jansen, K. E., Johan, Z., and Hughes, T. J. R., “Implementation of one-equation turbulence model within a stabilized finite element formulation of a symmetric advective-diffusive system,” *Computer Methods in Applied Mechanics and Engineering*, Vol. 105, 1993, pp. 405–433.
- [11] Shur, M. L., Spalart, P. R., Strelets, M. K., and Travin, A. K., “A hybrid RANS-LES approach with delayed-DES and wall-modeled LES capabilities,” *International Journal of Heat and Fluid Flow*, Vol. 29, 2008, pp. 1638–1649.
- [12] Buscaglia, G. C. and Dari, E. A., “Anisotropic mesh optimization and its application in adaptivity,” *International Journal for Numerical Methods in Engineering*, Vol. 40, 1997, pp. 4119–4136.
- [13] Casto-Diaz, M. J., Hecht, F., Mohammadi, B., and Pironneau, O., “Anisotropic unstructured mesh adaptation for flow simulations,” *International Journal for Numerical Methods in Fluids*, Vol. 25, 1997, pp. 475–491.
- [14] Peraire, J., Peiro, J., and Morgan, K., “Adaptive remeshing for three-dimensional compressible flow computation,” *Journal of Computational Physics*, Vol. 103, No. 2, 1992, pp. 269–285.
- [15] Pain, C. C., Umpleby, A. P., de Oliveira, C. R. E., and Goddard, A. J. H., “Tetrahedral mesh optimization and adaptivity for steady-state and transient finite element calculations,” *Computer Methods in Applied Mechanics and Engineering*, Vol. 190, 2001, pp. 3771–3796.

- [16] Li, X., Shephard, M. S., and Beall, M. W., “3D anisotropic mesh adaptation by mesh modifications,” *Computer Methods in Applied Mechanics and Engineering*, Vol. 194, 2005, pp. 4915–4950.
- [17] Sahni, O., Muller, J., Jansen, K. E., Shephard, M. S., and Taylor, C. A., “Efficient anisotropic adaptive discretization of the cardiovascular system,” *Computer Methods in Applied Mechanics and Engineering*, Vol. 195, No. 41–43, 2006, pp. 5634–5655.
- [18] “Simmetrix Inc.” <http://www.simmetrix.com>, 2013-05-20.
- [19] Spalart, P. R. and Allmaras, S. R., “A one-equation turbulence model for aerodynamic flows,” *AIAA paper 92-439*, 1992.
- [20] Spalding, D. B., “A single formula for the law of the wall,” *Journal of Applied Mechanics*, Vol. 28, 1961, pp. 455–458.
- [21] Huang, P. G., Coleman, G. N., and Bradshaw, P., “Compressible turbulent channel flows: DNS results and modelling,” *Journal of Fluid Mechanics*, Vol. 305, 1995, pp. 1485–218.
- [22] Spalart, P. R., “Trends in turbulence treatments,” *AIAA paper 2000-2306*, June 2000.
- [23] Spalart, P. R., “Young-person’s guide to detached-eddy simulation grids,” *NASA/CR-2001-211032*, National Aeronautics and Space Administration, 2001.
- [24] Ma, K.-L., Rosendale, J. V., and Vermeer, W., “3D shock wave visualization on unstructured grids,” San Fransisco, CA, October 1996, pp. 87–94.
- [25] Delery, J. M., “Investigation of strong shock turbulent boundary layer interaction in 2-D transonic flows with emphasis on turbulence phenomena,” *Proceedings of 14th Fluid and Plasma Dynamics conference*, American Institute of Aeronautics and Astronautics, 1981.
- [26] V. Schmitt and F. Charpin, “Pressure distribution on the ONERA-M6-Wing at transonic mach numbers,” *Report of the Fluid Dynamics Panel Working Group 04*, Vol. 138, AGARD, May 1979.
- [27] Whiting, C. H., Jansen, K. E., and Dey, S., “Hierarchical basis in stabilized finite element methods for compressible flows,” *Computer Methods in Applied Mechanics and Engineering*, Vol. 192, 2003, pp. 5167–5185.
- [28] Emory, M., Pecnik, R., and Laccarino, G., “Modeling structural uncertainties in Reynolds-averaged computations of shock/boundary layer interactions,” *AIAA paper 2011-0479*, 2011.
- [29] Len, F. S. and Kalitzin, G., “Computations of transonic flow with  $v^2-f$  turbulence model,” *International Journal of Heat and Fluid Flow*, Vol. 22, 2001, pp. 53–61.